

# A CMOS Timer-Injector Integrated Circuit for Self-Powered Sensing of Time-of-Occurrence

Liang Zhou<sup>1</sup>, Student Member, IEEE, Kenji Aono<sup>2</sup>, Member, IEEE,  
and Shantanu Chakrabartty<sup>3</sup>, Senior Member, IEEE

**Abstract**—Self-powered sensing of the time-of-occurrence of an event is challenging, because it requires access to a reliable time reference or a synchronized clock. In this paper, we propose for the first time a self-powered integrated circuit that is capable of time-stamping asynchronous mechanical events of interest. The core of the proposed design is the integration of two self-powered modules: 1) a chip-scale Fowler–Nordheim tunneling-based timer array, for generating a precision, relative time reference; and 2) a linear piezoelectricity-driven hot-electron injector acting as a floating-gate memory to record the onset of mechanical events. This paper presents measured results from a  $4 \times 4$  fully programmable timer array system-on-chip (SoC) and a linear injector array SoC, both of which have been prototyped in a standard double-poly CMOS process. The synchronization error of the timer array with respect to an external software clock was measured to be less than 1% over a duration of 100 h, and the average accuracy in sensing the time-of-occurrence of the event was measured to be 6.9%. The minimum activation energy of the self-powered system was measured to be 840 nJ (measured for event durations of 1 s), which is significantly lower than the energy that can be harvested from typical mechanical impacts.

**Index Terms**—Floating-gate, piezo-floating-gate sensors, self-powered systems, time reference, time-of-occurrence.

## I. INTRODUCTION

**S**ELF-POWERING of integrated circuits is attractive for sensing applications where the availability of energy is scarce, for instance, embedded or implantable applications [1]–[6] or for applications where large-scale remote powering is not practical, such as passive Internet of Things [7]–[9]. Unlike conventional energy scavenging systems, self-powered sensors scavenge their operational energy directly from the signal being sensed, thus obviating the need for periodic sampling or wake-up interrupts. For example, the self-powered sensor-data-logger, which was proposed in [10] and [11], harvested the energy from a mechanical

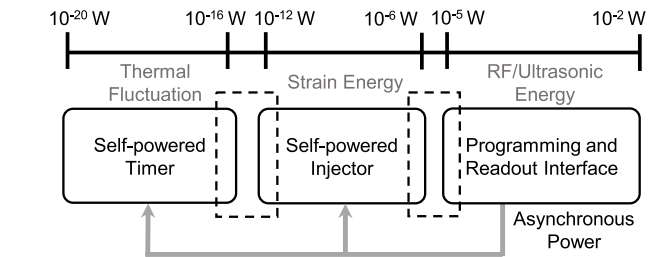


Fig. 1. Multi-scale power requirements for self-powered sensing of event time-of-occurrence.

event to store and update the event statistics on a non-volatile memory. Unfortunately, compared with a conventional interrupt-based paradigm, the asynchronous self-powering paradigm is unable to sense the time-of-occurrence for an event. This is due to the unavailability of a time reference or a watch-dog clock [12]–[15], both of which require continuous powering. In [16] and [17], we proposed using the long-term electron-leakage process through gate oxide as a mechanism for continuous time-keeping. A trap-assisted electron-leakage device was proposed in [16] and shown to be operational for durations greater than 100 h. However, the unpredictability in the oxide-trap locations resulted in significant device mismatch and hence poor temporal synchronization between different timer devices. In [17] a Fowler–Nordheim (FN)-tunneling-based time-keeping device was proposed, and the long-term dynamics was demonstrated to be stable and robust to device mismatch and temperature variations.

In this paper, we exploit the reliable time-keeping ability of an FN-timer device to design a fully integrated self-powered system that is capable of sensing time-of-occurrence of an event. Even though the proposed self-powered architecture is applicable for different sensing modalities, the focus of this paper will be on time stamping of mechanical events, for example physical impact [18]–[21] or changes in structural strain [22], [23]. The architecture of the proposed system is shown in Fig. 1 and comprises three system modules:

- 1) *Self-Powered Timer*: It will serve as a source of a precision time reference over a desired monitoring period. Since the monitoring period could be more than three years, the power levels at which a chip-scale time-keeping device needs to operate (using only the energy

Manuscript received September 6, 2017; revised November 16, 2017; accepted January 7, 2018. Date of publication January 30, 2018; date of current version April 23, 2018. This paper was approved by Associate Editor Dennis Sylvester. This work was supported by the National Science Foundation under Grant ECCS-1550096, Grant DGE-0802267, and Grant DGE-1143954. (Corresponding author: Shantanu Chakrabartty.)

L. Zhou and K. Aono are with the Department of Computer Science and Engineering, Washington University in St. Louis, St. Louis, MO 63130 USA.

S. Chakrabartty is with the Department of Electrical and Systems Engineering, Washington University in St. Louis, St. Louis, MO 63130 USA (e-mail: shantanu@wustl.edu).

Color versions of one or more of the figures in this paper are available online at <http://ieeexplore.ieee.org>.

Digital Object Identifier 10.1109/JSSC.2018.2793531

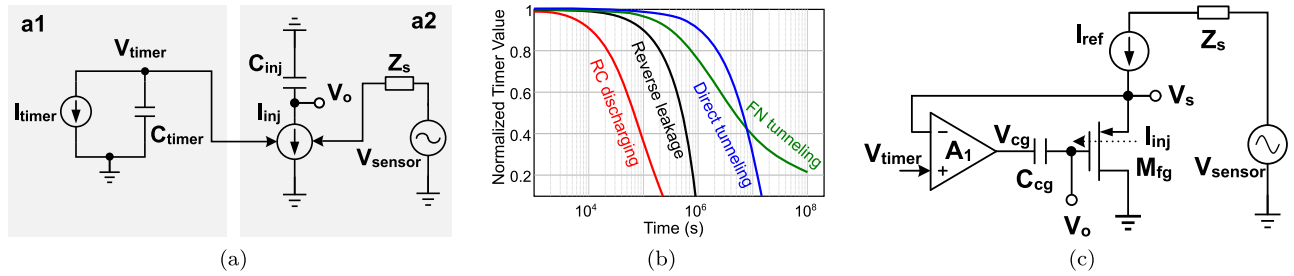


Fig. 2. Principle of operation of the proposed time-injector circuit. (a) Equivalent timer and injector circuits. (b) Comparison of discharge characteristics for different timer implementations. (c) Structure of a linear impact-ionized hot-electron injector.

stored on an integrated capacitor) have to be below an atto-watt (or  $10^{-18}$  W). The FN-timer device can operate at this power level, because it exploits a self-compensating physics of electron tunneling through a triangular FN barrier to implement a precision time reference.

- 2) *Self-Powered Injector*: While thermodynamic and quantum fluctuations could potentially be used to implement system clocks and timers, the energy is too scarce for sensing, computation, or data storage. In the proposed system, we combine the operational primitives of the FN timers with the physics of a piezoelectricity-driven impact-ionized hot-electron injector (p-IHEI) device [11], [20], [24]–[26] to time stamp mechanical events and for non-volatile storage within a pico-watt to nano-watt power budget.
- 3) *Programming and Readout Interface*: While FN-tunneling and strain-based self-powering might be sufficient for time stamping, sensing, computation, and non-volatile storage, it is not sufficient for initialization, calibration, or transfer of the stored measurements. In this regard, asynchronous powering, calibration, and readout could be achieved using a dedicated plug-and-play interface [20], [21] or a wireless radio-frequency [10] or ultrasound [27] interface. Since the focus of this paper is only on event time stamping, we will use a wired plug-and-play interface to demonstrate the functionality of the system.

## II. OPERATIONAL PRINCIPLE OF TIMER-INJECTOR

The principle of operation for the proposed time-of-occurrence sensing circuit is illustrated using an equivalent circuit model, as shown in Fig. 2(a). The time reference is implemented using the circuit a1, where a current sink  $I_{timer}$  discharges a pre-charged capacitor  $C_{timer}$ . As a result, the change in voltage  $V_{timer}$  serves as an indicator of the elapsed time.  $V_{timer}$  then modulates another current sink  $I_{inj}$ , as shown in the circuit a2 of Fig. 2(a), which discharges another capacitor  $C_{inj}$ . Because the current  $I_{inj}$  is supplied by the energy from a sensor transducer, the change in voltage  $V_o$  across  $C_{inj}$  encodes the time-of-occurrence of the event when the sensor was activated.

However, implementing a reliable time reference by exploiting the discharge characteristics on a capacitor is challenging, because it requires a precise on-chip discharge current sink

$I_{timer}$  that is continuously active for durations greater than three years. For example, ensuring a 1-V change across a 1-pF on-chip capacitance over a duration of one year would require a discharge current of  $3.2 \times 10^{-20}$  A (equivalent to a rate of ten electrons per minute). In Fig. 2(b), we show typical discharge characteristics that can be achieved using different types of leakage elements, including a prohibitively large leakage resistance of  $10^{18} \Omega$ . Reverse-leakage currents across standard p-n junctions are too large (on the order of femtoamperes), and any active cancellation mechanisms to achieve atto-watt leakage [28] would require external powering. Direct tunneling of electrons through the gate-oxide could potentially approach the desired discharge rate; however, the underlying translinear response is too steep [as shown in Fig. 2(b)] and is determined by process parameters (for example, oxide-thickness). In [17], we demonstrated that FN tunneling of electrons through a gate-oxide barrier can achieve the desired long-term discharge characteristics, as shown in Fig. 2(b). In [17] we also demonstrated that the response of a basic FN-timer device is reliable over durations up to three years and is robust to fabrication mismatch. In this paper, we use this basic FN-tunneling device to implement a chip-scale precision time reference and design a self-powered system for sensing event time-of-occurrence. Following the derivation given in [17] using an empirical expression of the FN-tunneling current  $I_{timer}$ , the timer output  $V_{timer}(t)$  can be expressed as:

$$V_{timer}(t) = \frac{k_2}{\ln(k_1 t + k_0)} + V_{sub}, \quad (1)$$

where  $k_0$ ,  $k_1$ , and  $k_2$  are the model parameters determined by the device form factors, initial conditions, and process parameters, and  $V_{sub}$  is the equivalent voltage drop at the substrate of the device. Details of the derivation and definitions of the model parameters can be found in [17] and are omitted here.

The circuit a2 in Fig. 2(a) can be implemented using an impact-ionized hot-electron injection on a floating-gate (FG), which is a polysilicon strip that is completely insulated by high-quality silicon dioxide. This mechanism is more suitable than other possible implementations of a2, because: 1) the floating-gate acts as a non-volatile storage element, and therefore, any injected charge is retained during the state when the timer-injector is unpowered and 2) the physics of impact-ionized hot-electron injection matches the physics

where  $C_{Tr}$  is the total capacitance seen from the gate node of  $M_{fgr}$ , including  $C_{cgr}$  and gate capacitance of  $M_{fgr}$ . Note that the initial charge  $Q_{fgr}$  and hence  $V_{fgr}$  can be programmed to be within the nominal input dynamic range of the readout circuits where the leakage is negligible [25]. Since  $Q_{fgr}$  can be assumed to be constant,  $V_{fgr}$  shows linear dependence on  $V_{fg}$ .

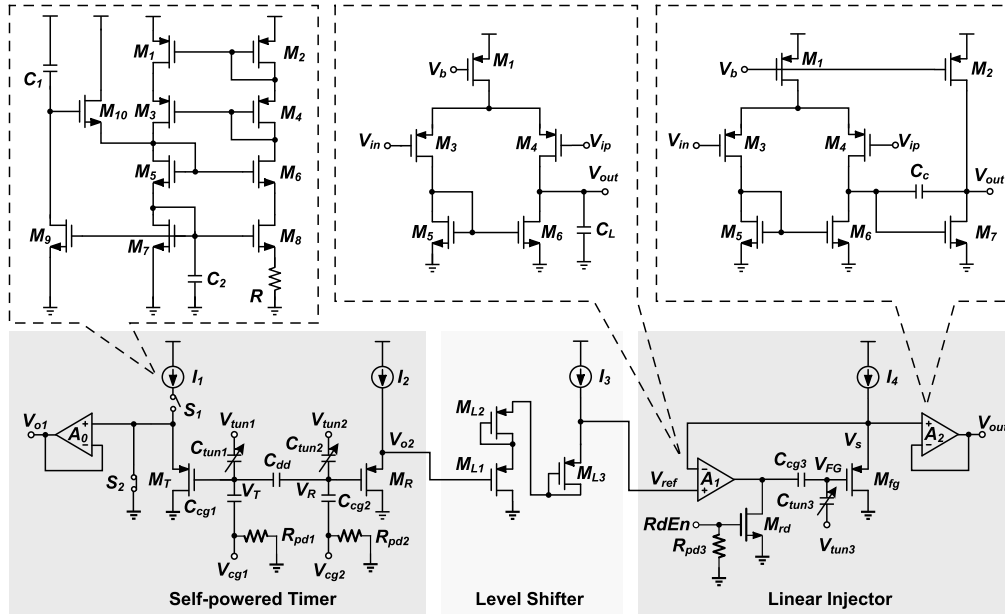


Fig. 4. Integration of the timer and injector circuit shown with respective programming switches, pull-down resistors, and schematic implementation of basic components (shown in the inset).

### B. Timer-Injector Circuit Implementation

The integration of the timer and the p-IHEI circuit is shown in Fig. 4 along with their respective programming, readout, and calibration switches.  $M_T$  and  $C_{cg1}$  form the floating-gate transistor, which functions as the timer device, and the timer readout circuit (capacitive divider and source-follower) is formed by  $M_R$ ,  $I_2$ ,  $C_{dd}$ , and  $C_{cg2}$ , which provides access to the timer voltage  $V_T$  through  $V_R$  and  $V_{o2}$ . A unity-gain buffer  $A_0$  is used for calibrating the response curve between  $V_{o1}$  and  $V_{o2}$ , hence between  $V_T$  and  $V_R$ , based on (8) as

$$V_{o1} = c_1 \cdot V_{o2} + c_0. \quad (9)$$

Here,  $c_1$  and  $c_0$  are determined by the initial conditions and value of the capacitors  $C_{cg1}$ ,  $C_{dd}$ , and  $C_{cg2}$ . The circuit also shows the pull-down resistors  $R_{pd1}$  and  $R_{pd2}$ , which ensure that the nodes are in a well-defined state when unpowered. A level shifter formed by pMOS transistors  $M_{L1}$ – $M_{L3}$  is used to match the output dynamic range of the timer to the input range of the linear injector, which is three times higher than that of a pMOS source-to-gate voltage  $V_{o2}$ . The linear injector feedback amplifier  $A_1$  sets the source voltage of the injection transistor  $M_{fg}$  as  $V_s \approx V_{ref} \approx V_{o2} + 3V_{sg}$ . The change in injection voltage  $V_{FG}$  is, therefore, a function of timer output  $V_{o2}$ .  $V_{FG}$  is read out by breaking the feedback loop using a pull-down transistor  $M_{rd}$ . In the readout configuration,  $M_{fg}$  and  $I_4$  act as a source-follower with  $V_s$  providing a measure of the stored floating-gate voltage  $V_{FG}$ . A unity-gain buffer  $A_2$  is used for isolating different linear injector cells and for driving the external readout circuits. The respective circuit-level implementation of the current sources  $I_1$ – $I_4$  and the buffers  $A_0$ – $A_2$  is shown in the top portion of Fig. 4.

Programming the floating-gate nodes  $V_T$ ,  $V_R$ , and  $V_{FG}$  uses a combination of FN tunneling and hot-electron injection. FN tunneling removes the electrons from the floating-gate

node by applying a high voltage ( $\geq 15$  V in 0.5- $\mu$ m CMOS process) across a parasitic nMOS capacitor  $C_{tun}$  ( $C_{tun1}$ – $C_{tun3}$  in Fig. 4). Although FN tunneling can be used to program FG memories individually [29], FN tunneling is typically used as a global programming, because the isolation of high voltages in a standard CMOS process is cumbersome. Hot-electron injection, on the other hand, requires lower voltage (4.2 V in 0.5- $\mu$ m CMOS process) than tunneling and, hence, is the preferred mechanism for precise programming of floating-gates. Because hot-electron injection in a pMOS transistor is a positive feedback process and can only be used to add electrons to the floating gate, the process needs to be carefully controlled and periodically monitored to ensure that the FG voltage is programmed to the desired value. The methods proposed in the literature [25] achieve desired value either by adjusting the duration for which the FG transistor is injected or by adjusting the magnitude of the injection pulses.

### C. System Implementation

A complete implementation of the self-powered timer-injector system is shown in Fig. 5, which contains the harvesting, programming, and configuration modules. The chip-scale time reference is comprised of a  $4 \times 4$  timer cell array, each of which could be selected using a decoder. A decoder module is used for initializing and reading the timer cells and for isolating defective cells and clustering the output of valid cells. Two charge pumps are integrated on the time-reference chipset to enable independent programming of  $V_T$  and  $V_R$  to a different initialization range. Note that for a 0.5- $\mu$ m CMOS process,  $V_T$  needs to be initialized to voltages greater than 8 V, whereas  $V_R$  needs to be initialized to voltages less than 3.3 V. The circuit-level implementation of the charge pumps have been previously reported in [10] and is shown in Fig. 5 (inset).



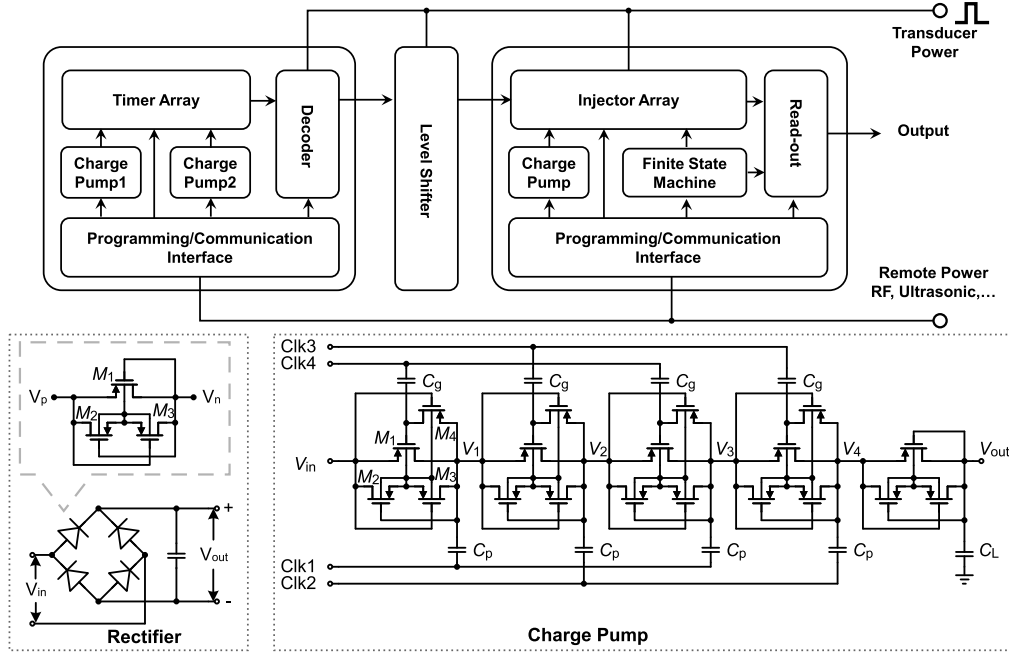


Fig. 5. System-level architecture and integration of the time-of-occurrence sensing system.

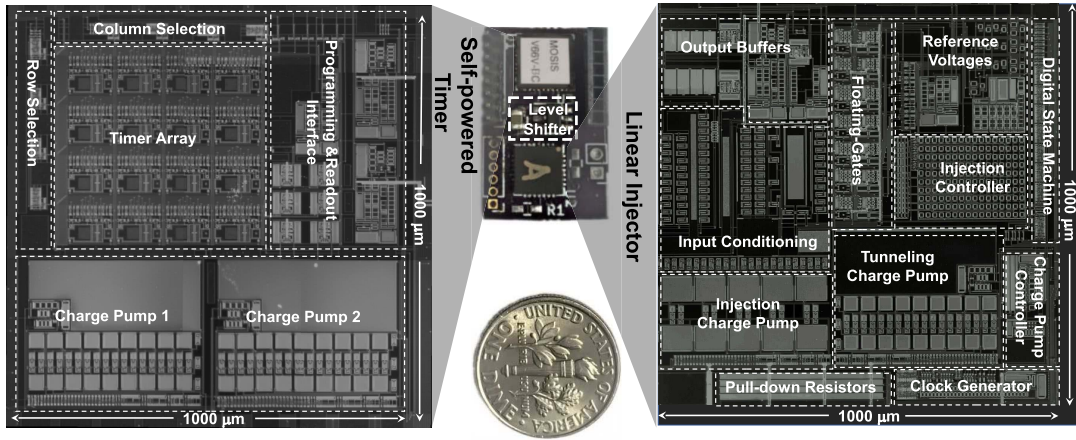


Fig. 6. Integration of the self-powered time-stamped sensor on a PCB and a die micro-photograph of the fabricated prototypes.

In the self-powered timing mode, the timer array continuously operates without any external power source, while during the mechanical event, the transducer signal provides power [through the full-wave rectifier shown in Fig. 5 (inset)] for the timer readout, the level shifter, and the linear injector. In this paper, we have emulated the mechanical event using an electrical pulse with a well-controlled pulse duration. Note that this approximation is valid as long as the duration of the event is significantly shorter than the total monitoring period. The system block of the linear injector is also shown in Fig. 5, where an on-chip charge pump is integrated for initializing the floating-gate values. A finite-state machine (FSM) functions as the control logic for channel readout and programming together with the programming and communication interface. The stored value on each of the injector channels can be accessed through a readout module. The energy required for programming and data transfer is provided through an external

plug-and-play, a radio-frequency, or an ultrasound interface. Circuit details of the programming, FSM and remote power transfer have been reported in [10], [20], and [21] and are omitted here for the sake of brevity.

#### IV. MEASUREMENT RESULTS

Due to the difference in operating voltage requirements, the timer and the linear injector have been implemented on two different silicon dies. The micrographs of both silicon dies are shown in Fig. 6, and the chipsets have been integrated onto a printed circuit board (PCB) with a level shifter acting as the interface circuitry. Separating the two substrates reduces the effect of substrate noise introduced by the power harvesting and charge-pump circuits in the linear injector. Also, isolating the timer and injector modules enables us to measure, calibrate, and program the two modules independent of each other. Both the modules occupy a  $1000 \times 1000 \mu\text{m}^2$  die area, and

TABLE I  
SPECIFICATIONS OF THE TIME-STAMPED SENSOR

Parameter	Value	
Technology	0.5 $\mu\text{m}$ CMOS	
PCB Size	1.4 $\times$ 2.2 cm <sup>2</sup>	
Die Sizes	2 $\times$ 1.5 $\times$ 1.5 mm <sup>2</sup>	
Timer Dynamic Range	0.3 V	
Injector Linear Range	1.2 V for 1.8 V supply	
Monitoring Period	up to 3 years	
Power for 6 V supply	Timer Read-out	300 nW
	Level Shifter	120 nW
	Linear Injector	420 nW
	Total	840 nW

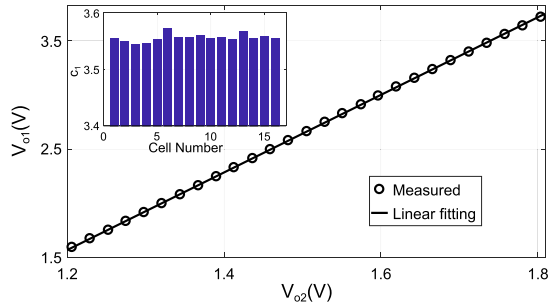


Fig. 7. Measured readout response of the timer: linear dependence between  $V_{o1}$  and  $V_{o2}$ , and distribution of coefficient  $c_1$ .

in Table I, we summarize key specifications of the prototype system.

#### A. Measured Timer-Array Response

The first set of experiments characterized the response of the timer array. Because each element of the array is accessed using a dual-floating-gate capacitive divider, as shown in Fig. 4, we characterized the dependence between the voltages  $V_T$  and  $V_R$  for different timer cells. By biasing  $V_T$  and  $V_R$  within a small readout range, we obtained the relationship between  $V_{o1}$  and  $V_{o2}$ , as shown in Fig. 7. The response shows a linearity larger than 50 dB, indicating that  $V_{o1}$  can be accurately estimated by measuring the voltage  $V_{o2}$ , which modulates the injector current. The inset of Fig. 7 shows the estimated calibration coefficient  $c_1$  for each cell in the timer array.  $c_1$  was estimated to be  $3.55 \pm 0.02$ , and the variation was found to be relatively small, and therefore, the average value of  $c_1$  could be used for calibrating the entire array.

The second group of experiments was conducted to measure the time-keeping ability of the timer cells in the array. We first programmed  $V_T$  of each timer cell to around 8.5 V implying an output of  $V_{o1}$  close to 9.5 V to initiate FN tunneling through the gate-oxide barrier. Fig. 8 plots the temporal responses of each of the 16 timer cells in the array, and the discharge characteristics conform to the model given in (1). Due to the mismatch in the threshold voltage of  $M_R$  and the FN-tunneling junction, the measured timer responses (and hence the parameters  $k_1$ ,  $k_2$ ,  $k_3$ , and  $V_{\text{sub}}$ ) would vary. As shown in Fig. 8, after the initial transient response, where the effects of mismatch are

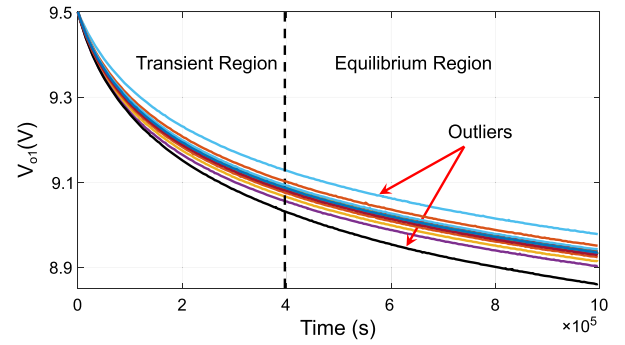


Fig. 8. Measured temporal response of the array with 16 cells.

more prominent, each of the timer cells enter an equilibrium region where the change in timer voltages are relatively robust with respect to one another. The physics of the equilibrium region is described in detail in [17] and are omitted here for the sake of brevity. As shown in Fig. 8, the measured responses are used to identify outliers of the timers. These timer cells are marked defective and disabled using the decoder.

In this paper, we combine the responses of multiple timer cells to improve the synchronization accuracy. To demonstrate this, we split the timers in the array into two clusters with equal number of cells, namely eight in this case. We chose four timers from each cluster such that the eight timers in each cluster were sorted according to their timer values, and only the middle four timers were kept and the remaining four were discarded. The timer responses corresponding to two separate cells operating in the equilibrium region are shown in Fig. 9(a), and the relative deviation with respect to each other is plotted in Fig. 9(c). The responses of the two timer clusters are plotted in Fig. 9(b), and the deviation with respect to the clusters is plotted in Fig. 9(d). The results show that the synchronization accuracy of the timer cluster is superior compared with the individual timer cell by a factor of two. The maximum deviation for the two clusters is measured to be less than 1.5 mV across a dynamic range of 150 mV, implying a synchronization accuracy better than 1% over a duration larger than 160 h, or approximately  $6 \cdot 10^5$  s.

#### B. Measured Linear Injector Response

Fig. 10 shows the measured linear response of the injector across a 1-V dynamic programming range. As shown in Fig. 10(a), the reduction of the floating-gate voltage shows a linear dependence with the injection duration, and Fig. 10(b) plots the programming accuracy of the linear injector. The maximum amplitude of the programming variation is less than 0.15 mV, which effectively gives 12.5-bit accuracy. We characterized the linearity for programming voltage  $V_s$  ranging from 4.5 V to 5.3 V, and in worst case, the linearity is around 11 bits, which is consistent with the results in [25] when considering the additional supporting circuitry, such as output buffers utilized in this design.

Besides the linearity, another key feature of the injector is the accuracy of the model expressed by (2).

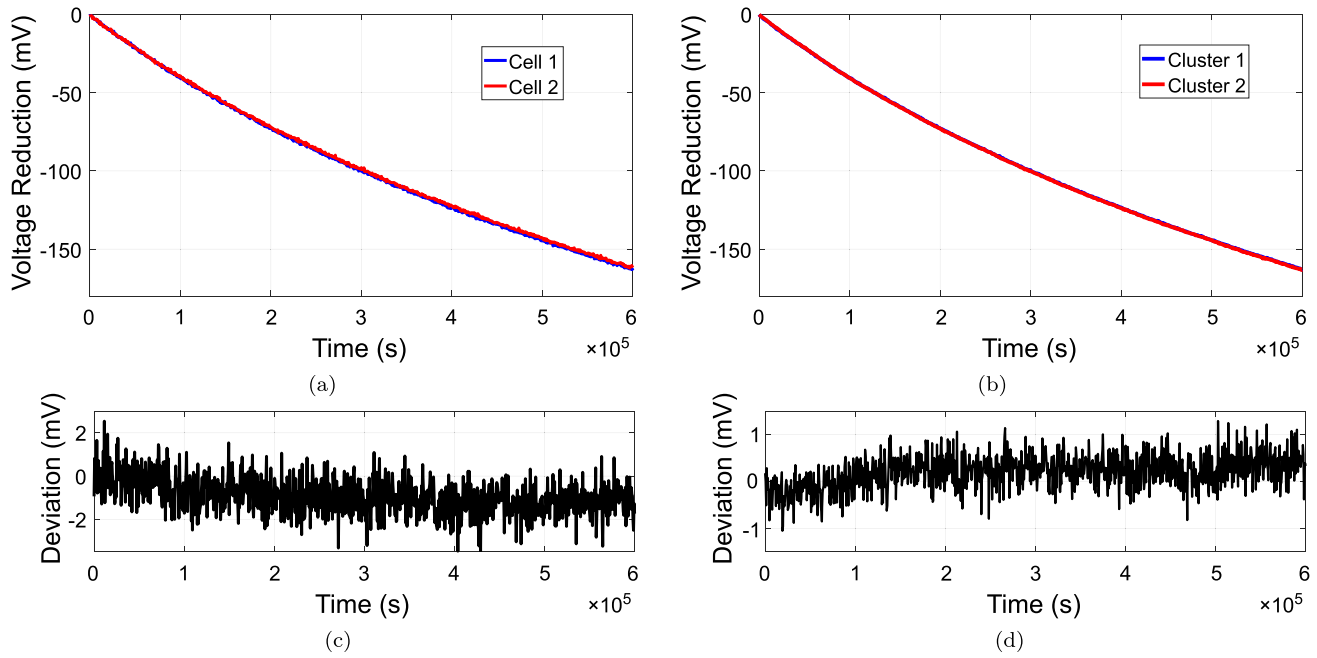


Fig. 9. Comparison of the timer's response with and without clustering. (a) Response of two timer cells in the equilibrium region. (b) Response of two clusters derived from the 16 cells. (c) Deviation between the two cells response. (d) Deviation between the response of the two clusters.

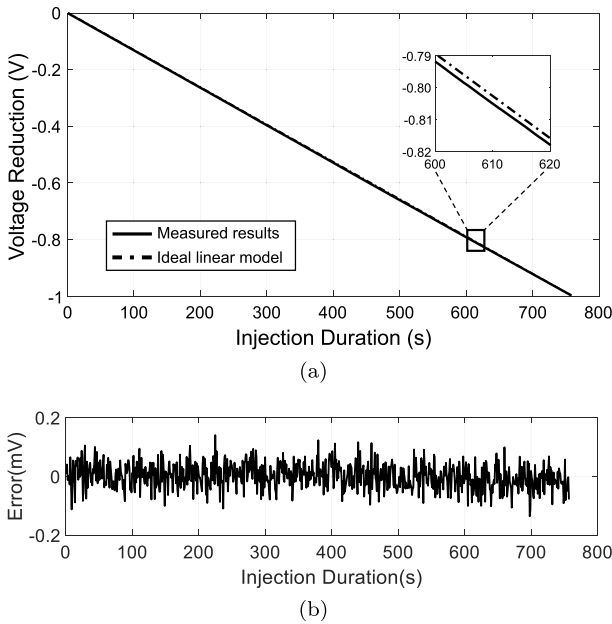


Fig. 10. Measured linear injector's response showing. (a) Linear dependence of the injection voltage on the programming duration at  $V_{ref} = 4.8$  V and  $I_s = 20$  nA. (b) Difference between the measured results and the linear model.

The recovery of the time depends on the accuracy of the model. To characterize it, we measured the injection rate at different injection reference voltages, and the results are plotted in Fig. 11. The fitted data using the model of (2) are plotted as the solid line, and the measured data are denoted with a circle. As evident, the measured data are strongly correlated with the fit model across the injection voltage reference range 4.5–5.3 V.

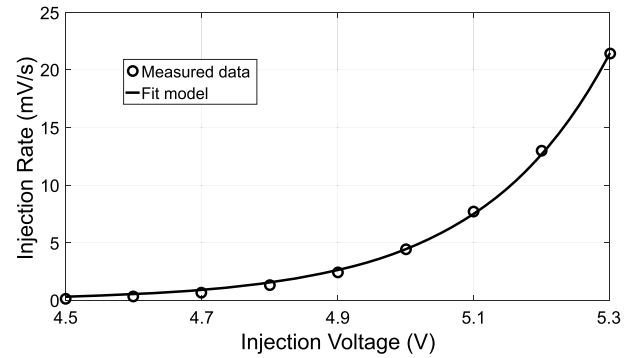


Fig. 11. Dependence of injection rate on source-to-drain voltage.

### C. Time-of-Occurrence Measurement

The next group of experiments was designed to validate the ability of the system to time stamp events. As shown in Fig. 4, the reference terminal  $V_{ref}$  of the injector was connected to the level-shifted timer output. To emulate a mechanical event, the transducer input to the system (as shown in Fig. 5) was powered every 10 min for a duration of 1 s. The choice of the event duration is reasonable and has been validated previously for different real-world mechanical event monitoring scenarios [6], [10], [11], [21]. This process of powering was repeated for 3000 min (or  $1.8 \cdot 10^5$  s). The measured data were randomly split into two groups: 200 points for calibrating the model parameters in (4) and the remainder of the 100 points as a test set for verifying the model accuracy. Fig. 12(a) shows the training data points marked with black dots, and the red line tracks the trained model expressed by (4). This model was used to predict when a specified event occurred for the data in the test set. Fig. 12(b) shows

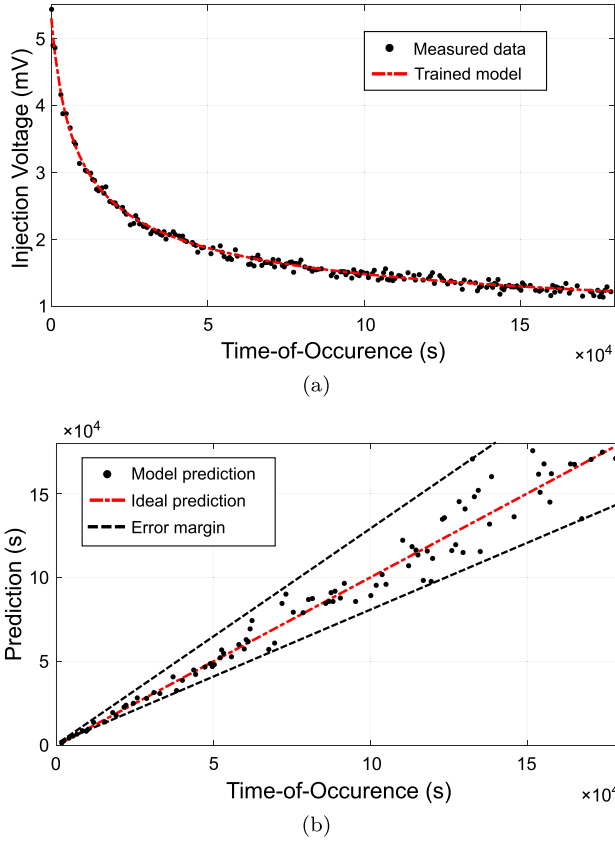


Fig. 12. Training and testing using the measured response from the time-stamped injector. (a) Data used for training marked as dot and the trained model plotted as red line. (b) Predicted time using testing data marked with a dot.

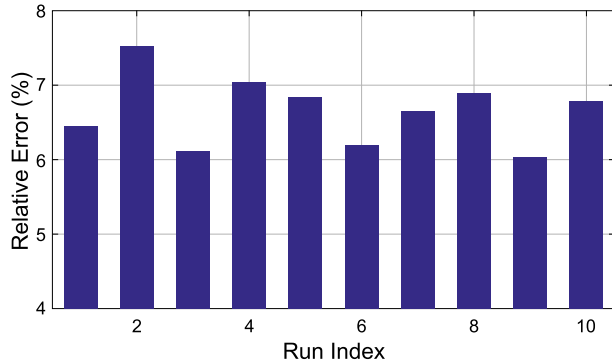


Fig. 13. Relative time recovery accuracy across multiple runs.

the predicted time with respect to the true time-of-occurrence for the test set, where the red dashed line indicates the ideal prediction. Based on the measured results, the average relative time recovery accuracy is calculated to be 6.9% across 50 h ( $1.8 \cdot 10^5$  s) of operation. The error margin plotted as a dashed line indicates the worst case accuracy in predicting time-of-occurrence. Here, the average accuracy is defined as

$$\text{Average\_accuracy} = \frac{1}{N} \sum_{i=1}^N \left| \frac{\tilde{t}_i - t_i}{t_i} \right| \quad (10)$$

where  $\tilde{t}_i$  is the recovered time at time instant  $t_i$ .

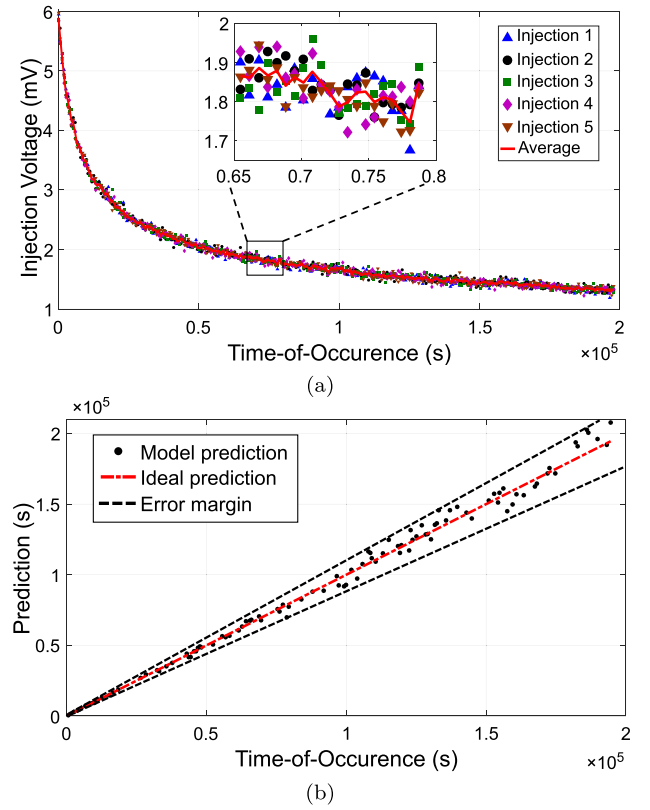


Fig. 14. Using averaging to improve the time-of-occurrence estimation. (a) Measured response of five injections at the same time instant and average response across the five measurements. (b) Predicted time using the average data for higher accuracy (the average relative accuracy is 3.2%).

Another group of experiments was conducted to verify the robustness and reliability of the proposed time-stamping procedure. Using the aforementioned process, with the same event activation frequency and duration, the average relative error for each test set is shown in Fig. 13. The relative accuracy across ten independent runs falls within 6%–8%, demonstrating reliable recovery performance.

The model of (4) indicates that the sensed value is a function of source current  $I_s$ , injection reference  $V_{\text{ref}}$ , and the injection duration  $\Delta t$ , which implies that any noise introduced into these three parameters will affect the reconstruction accuracy. For instance, the source current shows the dependence on the temperature and power supply variations. The output of the level shifter is also a function of environmental variations, such as temperature and RF coupling. The injection duration shows random variations due to the intrinsic circuit start-up time, the pulse duration error introduced by the programming interface, and so forth. For these small random fluctuations, techniques, such as averaging, enlarging the injection duration, and tighter program control, could help improve the reconstruction accuracy.

To validate the impact of random noise and variations, we conducted the time-stamping experiment using an averaging technique. For each time instant, we activate five of injector channels and recorded the measured output. Fig. 14(a) plots the measured data points for each injection and the average value across all the injections. As can be seen,



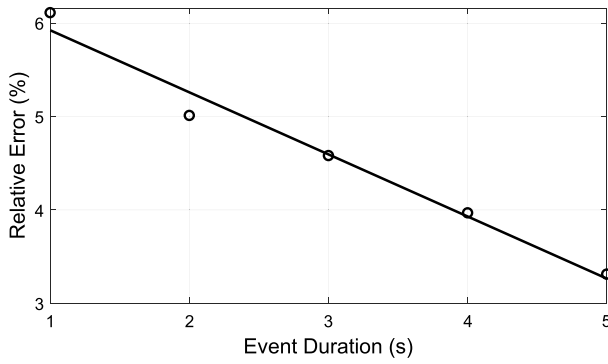


Fig. 15. Dependence of relative time-of-occurrence estimation accuracy on the event duration.

the variance of each injector output is larger than that of the average, as expected. We further used the average output for parameter estimation and for time-of-occurrence prediction, and the result is shown in Fig. 14(b). The error margin is much closer to the ideal prediction than that shown in Fig. 12(b), and the relative accuracy is measured to be 3.2%, which is an improvement over 6.9% for the individual injection. This finding corroborates the hypothesis that one is able to improve the time recovery accuracy by using array implementations with multiple channels.

Another experiment was conducted to verify that the injection duration also affects time recovery accuracy. With a larger injection duration, the variations, such as the start-up time, will be proportionally small compared with the injection duration. The time-stamping experiment was conducted with event durations from 1 to 5 s, and the predicted accuracy for each duration is shown in Fig. 15. The results indicate that the relative error monotonically decreases with the increase of the injection duration, which validates the assumption regarding accuracy and injection duration. This result also suggests that we can improve the time recovery accuracy by extending the duration of the event, possibly using our previous reported time-dilation technique [21], [26].

## V. DISCUSSION

Because the total current consumption of our circuit (when fully activated) is limited by the proportional-to-absolute-temperature (PTAT) current reference to 140 nA, the load to the mechanical (piezoelectric) transducer can be considered as a current sink. Under this condition, the voltage generated at the output of the transducer is indicative of the input power. Also, hot-electron injection in this CMOS process requires a minimum of 4.2-V drop across the source and the drain terminal of the floating-gate transistor. Thus, there is a minimum voltage requirement for the proposed sensor to log the occurrence of a mechanical event. As long as this minimum power and additional power to activate the measurement circuitry (total of 840 nW) are available from the mechanical event, the nature of the mechanical event need not be repeatable. For a single event with a duration of 1 s, the total energy required would be 840 nJ—significantly smaller than what are available from mechanical impacts. When the available energy is much higher than the energy that can be consumed by the sensor circuitry, an energy buffering front end is required to

accurately measure the magnitude of the impact. An example of this is our previously reported time-dilation circuitry used for harvesting energy from head impacts [21]. Note that once the energy is successfully buffered, a wide variety of data logging options are available, including the use of a low-power analog-to-digital converter and a non-volatile memory. This can help improve the accuracy of the time-of-occurrence measurement.

With regard to estimating the time-of-occurrence, four types of errors could affect the accuracy. The first is due to the thermal noise in the measurement circuits. This can be mitigated by choosing a larger injection duration that averages the errors, and the sensitivity analysis summarized in (7) highlights the degree of mitigation. The second source of error is due to the start-up, which is determined to be in the range of a few milliseconds. While we have assumed an event duration of 1 s, the actual time of injection is less than 1 s due to the inherent delay in the start-up circuits. The systematic part of the startup time will be absorbed by the  $\Delta t$  term of (6), and it does not affect the accuracy; nonetheless, the random part will degrade the time recovery accuracy. As discussed in Section IV, this type of noise is random and can be mitigated by a larger injection duration or averaging technique. The third type of error source is model accuracy. Both models developed for the timer and the injector consider only the first-order effects and neglect the high-order effects' impact. For the timer model, the image charge barrier effect is neglected for model derivation. For the linear injector model, the finite gain of the feedback amplifier will result in a model mismatch in the second order. As a result, the model will introduce a systematic error to the time recovery process. Although beyond the scope of this paper, leveraging machine learning could allow for more precise and accurate models to improve the time recovery accuracy. The last factor that could affect the time recovery accuracy is temperature. In this paper, the current generated by the PTAT current source has a strong temperature dependence, which will affect the timer readout and injection rate. This issue can be resolved either by using a bandgap reference or using temperature dependent  $R$  in Fig. 4 to compensate the temperature effect. The impact of the temperature on timer response was analyzed in [17], and Fig. 16 shows the dependence of timing accuracy of the timer on temperature. They are predicted using the model derived from the measured results at a constant temperature of 20 °C. The results show that the variations in the predicted time due to small temperature fluctuations are linear, and thus, small statistical variations in temperature can be averaged out. However, long-term temperature drifts cannot be averaged out, and temperature drift of one degree will introduce approximately one percent error in the timing accuracy. Since the timer is completely self-powered, active temperature compensation is infeasible here. Our future work will focus on exploiting differential response in an array of timers to compensate for temperature.

The lifetime of self-powered sensors can span several years, which requires a timing device that can operate on the same time scale. The literature [17] verified that the proposed timer device can operate as long as three years. However,

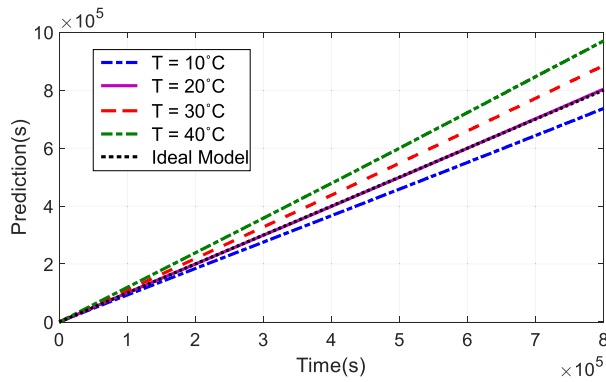


Fig. 16. Dependence of the timing accuracy on temperature.

there is a tradeoff between the operational lifetime and the time accuracy. As shown in Fig. 8, the timer output has a nonlinear dependence with respect to time and exhibits a saturating behavior. This leads to weaker dependence of the injection voltage on time and thus a lower accuracy in time. A potential solution to this issue is to use multiple timers and use some ensemble statistics of their outputs, which will improve the accuracy, albeit at the cost of chip area and power. Also in this implementation, the capacitor divider used in the readout circuit reduces the dynamic range of the timer by a factor of 0.28. Thus, the dynamic range can be improved by exploring a different capacitor divider topology or by exploring other potential readout circuits that can reduce the effect of signal attenuation. Note that the calibration time (3000 min in this paper, or  $1.8 \cdot 10^5$  s) can be reduced to a few minutes by biasing the timer at a higher level ( $> 10$  V). However, this will degrade the timing accuracy due to the error incurred in the parameter estimation.

## VI. CONCLUSION

In this paper, we proposed a novel architecture and a system-on-chip implementation of a self-powered system that is capable of sensing time-of-occurrence of events. The system uses a chip-scale self-powered time-reference array that can continuously operate without any external powering. By combining the timing device with a linear hot-electron injector array, the time-injector circuit can record both the event and the time-of-occurrence and store the information on a non-volatile floating-gate memory. The measured results from fabricated and integrated timer-injector prototypes show that the circuit can sense time-of-occurrence of an event with an average accuracy of 6.9% across a two-day monitoring period for events with a duration of 1 s. The total power consumption of the system is optimized to less than 1 mW, which makes it feasible for self-powering using different types of piezoelectric transducers.

## REFERENCES

- [1] V. Giurgiutiu, A. Zagari, and J. J. Bao, "Piezoelectric wafer embedded active sensors for aging aircraft structural health monitoring," *Struct. Health Monitor.*, vol. 1, no. 1, pp. 41–61, 2002.
- [2] S. R. Platt, S. Farritor, K. Garvin, and H. Haider, "The use of piezoelectric ceramics for electric power generation within orthopedic implants," *IEEE/ASME Trans. Mechatronics*, vol. 10, no. 4, pp. 455–461, Aug. 2005.
- [3] N. Lajnef, N. G. Elvin, and S. Chakrabarty, "A piezo-powered floating-gate sensor array for long-term fatigue monitoring in biomechanical implants," *IEEE Trans. Biomed. Circuits Syst.*, vol. 2, no. 3, pp. 164–172, Sep. 2008.
- [4] E. Sazonov, H. Li, D. Curry, and P. Pillay, "Self-powered sensors for monitoring of highway bridges," *IEEE Sensors J.*, vol. 9, no. 11, pp. 1422–1429, Nov. 2009.
- [5] H. Chen *et al.*, "Low-power circuits for the bidirectional wireless monitoring system of the orthopedic implants," *IEEE Trans. Biomed. Circuits Syst.*, vol. 3, no. 6, pp. 437–443, Dec. 2009.
- [6] W. Borchani, K. Aono, N. Lajnef, and S. Chakrabarty, "Monitoring of postoperative bone healing using smart trauma-fixation device with integrated self-powered piezo-floating-gate sensors," *IEEE Trans. Biomed. Eng.*, vol. 63, no. 7, pp. 1463–1472, Jul. 2016.
- [7] L. Atzori, A. Iera, and G. Morabito, "The Internet of Things: A survey," *Comput. Netw.*, vol. 54, no. 15, pp. 2787–2805, Oct. 2010.
- [8] S. Amendola, R. Lodato, S. Manzari, C. Occhiuzzi, and G. Marrocco, "RFID technology for IoT-based personal healthcare in smart spaces," *IEEE Internet Things J.*, vol. 1, no. 2, pp. 144–152, Apr. 2014.
- [9] R. A. Potyralo, N. Nagraj, Z. Tang, F. J. Mondello, C. Surman, and W. Morris, "Battery-free radio frequency identification (RFID) sensors for food quality and safety," *J. Agricult. Food Chem.*, vol. 60, no. 35, pp. 8535–8543, 2012.
- [10] C. Huang and S. Chakrabarty, "An asynchronous analog self-powered CMOS sensor-data-logger with a 13.56 MHz RF programming interface," *IEEE J. Solid-State Circuits*, vol. 47, no. 2, pp. 476–489, Feb. 2012.
- [11] L. Zhou, A. C. Abraham, S. Y. Tang, and S. Chakrabarty, "A 5 nW quasi-linear CMOS hot-electron injector for self-powered monitoring of biomechanical strain variations," *IEEE Trans. Biomed. Circuits Syst.*, vol. 10, no. 6, pp. 1143–1151, Dec. 2016.
- [12] Y.-S. Lin, D. Sylvester, and D. Blaauw, "A sub-pW timer using gate leakage for ultra low-power sub-Hz monitoring systems," in *Proc. IEEE Custom Integr. Circuits Conf. (CICC)*, Sep. 2007, pp. 397–400.
- [13] Y. Lee, B. Giridhar, Z. Foo, D. Sylvester, and D. B. Blaauw, "A sub-nW multi-stage temperature compensated timer for ultra-low-power sensor nodes," *IEEE J. Solid-State Circuits*, vol. 48, no. 10, pp. 2511–2521, Oct. 2013.
- [14] A. Shrivastava and B. H. Calhoun, "A 150 nW, 5 ppm/°C, 100 kHz on-chip clock source for ultra low power SoCs," in *Proc. IEEE Custom Integr. Circuits Conf. (CICC)*, Sep. 2012, pp. 1–4.
- [15] H. Asano *et al.*, "A 1.66-nW/kHz, 32.7-kHz, 99.5 ppm/°C fully integrated current-mode RC oscillator for real-time clock applications with PVT stability," in *Proc. IEEE Conf. 42nd Eur. Solid-State Circuits Conf. (ESSCIRC)*, Sep. 2016, pp. 149–152.
- [16] L. Zhou, P. Sarkar, and S. Chakrabarty, "Scavenging thermal-noise energy for implementing long-term self-powered CMOS timers," in *Proc. IEEE Int. Symp. Circuits Syst. (ISCAS)*, May 2013, pp. 2203–2206.
- [17] L. Zhou and S. Chakrabarty, "Self-powered timekeeping and synchronization using Fowler–Nordheim tunneling-based floating-gate integrators," *IEEE Trans. Electron Devices*, vol. 64, no. 3, pp. 1254–1260, Mar. 2017.
- [18] L. M. Gessel, S. K. Fields, C. L. Collins, R. W. Dick, and R. D. Comstock, "Concussions among United States high school and collegiate athletes," *J. Athletic Training*, vol. 42, no. 4, pp. 495–503, 2007.
- [19] J. J. Crisco *et al.*, "Frequency and location of head impact exposures in individual collegiate football players," *J. Athletic Training*, vol. 45, no. 6, pp. 549–559, 2010.
- [20] K. Aono, T. Covassin, and S. Chakrabarty, "Monitoring of repeated head impacts using time-dilation based self-powered sensing," in *Proc. IEEE Int. Symp. Circuits Syst. (ISCAS)*, Jun. 2014, pp. 1620–1623.
- [21] T. Feng, K. Aono, T. Covassin, and S. Chakrabarty, "Self-powered monitoring of repeated head impacts using time-dilation energy measurement circuit," *IEEE Trans. Biomed. Circuits Syst.*, vol. 9, no. 2, pp. 217–226, Apr. 2015.
- [22] Y. Hu, L. Huang, W. S. A. Rieutort-Louis, J. Sanz-Robinson, J. C. Sturm, S. Wagner, and N. Verma, "A self-powered system for large-scale strain sensing by combining CMOS ICs with large-area electronics," *IEEE J. Solid-State Circuits*, vol. 49, no. 4, pp. 838–850, Apr. 2014.

- [23] Y. Guo, C. Aquino, D. Zhang, and B. Murmann, "A four-channel,  $\pm 36$  V, 780 kHz piezo driver chip for structural health monitoring," *IEEE J. Solid-State Circuits*, vol. 49, no. 7, pp. 1506–1513, Jul. 2014.
- [24] C. Huang, N. Lajnef, and S. Chakrabarty, "Calibration and characterization of self-powered floating-gate usage monitor with single electron per second operational limit," *IEEE Trans. Circuits Syst. I, Reg. Papers*, vol. 57, no. 3, pp. 556–567, Mar. 2010.
- [25] C. Huang, P. Sarkar, and S. Chakrabarty, "Rail-to-rail, linear hot-electron injection programming of floating-gate voltage bias generators at 13-bit resolution," *IEEE J. Solid State Circuits*, vol. 46, no. 11, pp. 2685–2692, Nov. 2011.
- [26] L. Zhou and S. Chakrabarty, "Linearization of CMOS hot-electron injectors for self-powered monitoring of biomechanical strain variations," *IEEE Trans. Biomed. Circuits Syst.*, vol. 11, no. 2, pp. 446–454, Apr. 2016.
- [27] S. H. Kondapalli, Y. Alazzawi, M. Malinowski, T. Timek, and S. Chakrabarty, "Multiaccess *in vivo* biotelemetry using sonomicrometry and M-scan ultrasound imaging," *IEEE Trans. Biomed. Eng.*, vol. 65, no. 1, pp. 149–158, Jan. 2017.
- [28] M. O'Halloran and R. Sarpeshkar, "A 10-nW 12-bit accurate analog storage cell with 10-aA leakage," *IEEE J. Solid-State Circuits*, vol. 39, no. 11, pp. 1985–1996, Nov. 2004.
- [29] L. Zhou and S. Chakrabarty, "A 7-transistor-per-cell, high-density analog storage array with 500  $\mu$ V update accuracy and greater than 60 dB linearity," in *Proc. IEEE Int. Symp. Circuits Syst. (ISCAS)*, Jun. 2014, pp. 1572–1575.



**Liang Zhou** (S'14) received the B.S. degree in physics from Tsinghua University, Beijing, China, in 2010. He is currently pursuing the Ph.D. degree with the Department of Computer Science and Engineering, Washington University in St. Louis, St. Louis, MO, USA.

His current research interests include low-power sensing systems, integrated biomedical sensors, analog, mixed-signal and RF circuits, and hardware security.

Mr. Zhou was a recipient of the Best Paper Award and the Honorary Mention for the Best Paper Award presented by the International Symposium on Circuits and Systems (ISCAS) in 2013 and 2015, respectively.



**Kenji Aono** (S'09–GS'11–M'17) received the B.S. degree in electrical engineering, the B.S. degree in computer engineering, and the M.S. degree in electrical engineering from Michigan State University, East Lansing, MI, USA, in 2011, 2011, and 2013, respectively. He is currently pursuing the Ph.D. degree in computer engineering from Washington University in St. Louis, St. Louis, MO, USA.

He was an NSF Graduate Research Fellow on tenure at Michigan State University and later at Washington University in St. Louis while pursuing the Ph.D. degree. In 2014, he was an NSF GROW Fellow stationed at The University of Tokyo, Tokyo, Japan.

Mr. Aono was an Officer of the Gamma Zeta Chapter of the IEEE Eta Kappa Nu and the IEEE Student Branch at Michigan State University. He was a recipient of the Michigan Space Grant Consortium Graduate Fellowship from 2012 to 2015. He was elected for roles in the IEEE Southeast Michigan Section, including the Chair of the Education Society and the Vice-Chair for Circuits and Systems and Young Professionals.



**Shantanu Chakrabarty** (S'99–M'04–SM'09) received the B.Tech. degree from IIT Delhi, New Delhi, India, in 1996, and the M.S. and Ph.D. degrees in electrical engineering from Johns Hopkins University, Baltimore, MD, USA, in 2002 and 2004, respectively.

From 1996 to 1999, he was with Qualcomm, Inc., San Diego, CA, USA. In 2002, he was a Visiting Researcher with The University of Tokyo, Tokyo, Japan. From 2004 to 2015, he was an Associate Professor with the Department of Electrical and Computer Engineering, Michigan State University (MSU), East Lansing, MI, USA. He is currently a Professor with the School of Applied Sciences and Engineering, Washington University in St. Louis, St. Louis, MO, USA. His current research interests include different aspects of analog computing, in particular non-volatile circuits, energy harvesting sensors, and neuromorphic and hybrid circuits and systems.

Dr. Chakrabarty was a Catalyst Foundation Fellow from 1999 to 2004. He was a recipient of the National Science Foundation's CAREER Award, the University Teacher-Scholar Award from MSU, and the 2012 Technology of the Year Award from MSU Technologies. He is currently serving as an Associate Editor of the IEEE TRANSACTIONS ON BIOMEDICAL CIRCUITS AND SYSTEMS and the *Advances in Artificial Neural Systems* journal and a Review Editor of the *Frontiers of Neuromorphic Engineering* journal.